ARTICLE

Exciton Dynamics in Edge-on ZnPc–F_8ZnPc System: Insights from Quantum Simulations†

Qiuyue Ge, Xunkun Huang, Yuchuan Xu, Wanzhen Liang*, Yi Zhao*

State Key Laboratory of Physical Chemistry of Solid Surfaces, iChEM, Fujian Provincial Key Laboratory of Theoretical and Computational Chemistry, and College of Chemistry and Chemical Engineering, Xiamen University, Xiamen 361005, China

(Dated: Received on June 26, 2025; Accepted on July 18, 2025)

Focusing on the mechanism of interfacial exciton dissociation in edge-on stacked ZnPc–F_8ZnPc aggregate, we employ the fragment particle-hole densities (FPHD) method to construct the Hamiltonian of diabatic states and use the non-Markovian stochastic Schrödinger equation (NMSSE) to simulate the photo-induced dynamics processes. The results show that aggregation effects have a significant impact on the interfacial exciton dissociation process. After photo-excitation, the excitons first preferentially delocalize and perform the charge transfer (CT) states in the pure ZnPc or F_8ZnPc aggregates within 100 fs. These 'intramolecular' CT states can easily evolve into interfacial CT states by hopping electrons and holes in the intramolecular CT states across the interface. Compared with these exciton dissociation processes, the direct exciton dissociation into interfacial CT state is relatively slow due to the small electronic coupling and vibrational coherence between the locally excited state and the interfacial CT state. As the temperature rises and the vibronic coherence weakens, the direct dissociation rates are significantly enhanced. This investigation provides valuable insights for the design and optimization of high-performance organic photovoltaic devices.

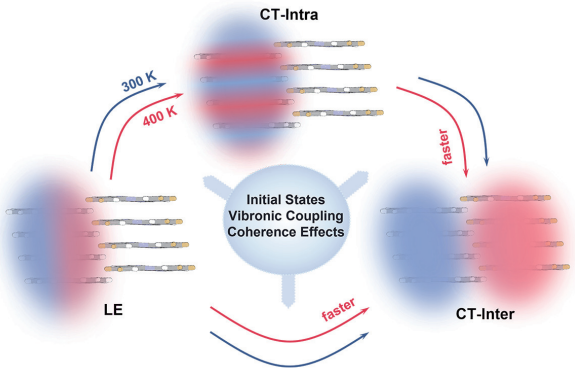

Key words: ZnPc–F_8ZnPc, Exciton dynamics, Coherence effects, Vibronic coupling effects

I. INTRODUCTION

With the rapid development of highly efficient organic photovoltaic cells, it has become extremely urgent to design and synthesize novel donor and acceptor materials with superior performance to further enhance the efficiency of organic photovoltaic devices [1–5]. Unlike single-component materials, multi-component materials containing donor and acceptor molecules can provide an effective driving force to overcome the Coulomb interactions between electrons and holes, which is conducive to improve the free carrier generation rate in organic photovoltaic cells [6–9]. However, a large energy offset at the donor–acceptor interface is not necessarily favorable for the photo-induced charge separation process and may even lead to significant energy loss [10]. The charge transfer state is generally regarded as an important intermediate in the process of exciton dissociation and charge separation after photo-excitation. Therefore, it is of great significance to study

† Part of Special Topic "Quantum Dynamics in Complex Systems".

* Authors to whom correspondence should be addressed.
E-mail: liangwz@xmu.edu.cn, yizhao@xmu.edu.cn

the CT state at the donor–acceptor interface.

The mechanism of photo-induced charge transfer in donor–acceptor systems has long been controversial. Some researchers have shown that photo-excitation can produce 'hot' excitons with excess energy, which can easily promote the separation of bound electron–hole pairs [11–13]. Others have suggested that photo-induced excitons first dissociate to form interfacial CT states, which then slowly separate further to form free carriers [14–16]. These two completely different charge separation pathways have been used to explain the dynamics processes in different practical systems. Some experimental results have shown that the generation of free carriers is independent of excitation energy. That is, the initial states with different energies have little effect on the free carrier generation rate [14, 17, 18] in donor–acceptor system. It has been reported that charge delocalization can significantly enhance charge mobility and reduce the Coulomb barrier [19–21]. Moreover, delocalization can also reduce the non-radiative voltage losses caused by charge recombination in organic solar cells [22, 23]. There are still debates on the process of exciton dissociation and the formation of charge separation states. Many influencing factors, such as the initial state [19], temperature effects [24], vibronic coupling effect [12, 25, 26], coherence effects [25, 27–29], need to be considered to further confirm their roles in charge transfer process.

Zinc phthalocyanine (ZnPc) and its fluorinated derivatives (F_8ZnPc) are commonly used as donor (D) and acceptor (A) materials in multi-component organic photovoltaic cells, respectively. Introducing highly electronegative fluorine atoms into the molecular backbone can enhance the electron-accepting ability of F_8ZnPc molecules [30–32]. Experimentally, directly introducing substituents into the molecular backbone to modulate molecular properties is an effective method to improve the performance of donor–acceptor materials. Previously, we used the face-on stacked ZnPc–F_8ZnPc system as the research object and investigated the dynamics process from the local excited (LE) states to the interfacial CT states and then to the charge separated (CS) states using different initial excited states, identifying several key factors that affect the power conversion efficiency of organic photovoltaic cells [33]. Through previous studies, we have analyzed in detail the effects of vibronic coupling and coherence on exciton dissociation into interfacial CT states in the face-on stacked ZnPc–F_8ZnPc system and demonstrated the promoting effect of the entropy on the generation of the CS states.

It has been reported experimentally that when a pair of D–A molecules switches from face-on to edge-on orientation, the CT-exciton heating process is reversed to a typical thermal CT-exciton cooling process [16]. Edge-on stacked aggregates form more pairs of DA interfaces compared to face-on stacked aggregates, which enables the simultaneous generation of more interfacial CT states. Therefore the edge-on orientation not only enhances the light absorption, but also improves the charge separation and transport efficiency, which in turn significantly improves the optoelectronic performance [34–36]. In this work, we study the exciton dissociation process in the edge-on stacked ZnPc–F_8ZnPc system using different stacking methods and analyze the effects of initial state, vibronic coupling effects, temperature effects, coherence effects on dynamics of the interfacial CT state.

Simulating the photo-induced exciton dynamics, involving various electronic excited states and complex intermolecular interactions in real systems, is quite complicated. To explicitly take into account the effects of the above mentioned complex factors, it is necessary to construct an aggregate model Hamiltonian that includes different types of excited states and then employ complex quantum dynamics methods combined with electronic structure calculations to simulate the photo-induced exciton dynamics. In our previous work [33, 37–42], we have demonstrated that the non-Markovian stochastic Schrödinger equation (NMSSE) based on the constructed aggregate model Hamiltonian can be used to investigate the vibrationally resolved electronic absorption spectra and photo-induced exciton dynamics of zinc phthalocyanine aggregates.

In this paper, we theoretically simulate the excited-state properties, vibrationally resolved electronic absorption spectra, and photo-induced exciton dynamics of ZnPc–F_8ZnPc aggregates in edge-on configuration. We aim to reveal the exciton dissociation mechanism of the ZnPc–F_8ZnPc system after photo-excitation. The structure of this paper is arranged as follows: Section II describes the theoretical methods, including the construction of the model Hamiltonian, the parameterization of the Hamiltonian, the introduction of the dynamics methods, and the details of the quantum chemical calculations. Section III presents the results and discussions, and Section IV is the conclusion.

DOI: 10.1063/1674-0068/cjcp2506086

II. THEORETICAL AND COMPUTATIONAL DETAILS

A. Effective model Hamiltonian for an aggregate system

Typically, electronic excitation energies and transition dipole moments are computed using electronic structure methods like time-dependent density functional theory (TD-DFT). However, these methods often operate within the electronic adiabatic representation, which complicates the identification of distinct electronic state characteristics. In this study, we employ a parameterized Hamiltonian in the diabatic representation including LE states, 'intramolecular' (hole and electron are localized on the same kind of molecules) CT states, and 'intermolecular' (hole and electron are localized on different kinds of molecules) CT states. The electronic and vibrational properties of an aggregate are described by the model Hamiltonian

$$\hat{H}_{\mathrm{agg}} = \hat{H}_{\mathrm{el}} + \hat{H}_{\mathrm{ph}} + \hat{H}_{\text{el-ph}}, \tag{1}$$

where $\hat{H}_{\mathrm{el}}$, $\hat{H}_{\mathrm{ph}}$, and $\hat{H}_{\text{el-ph}}$ stand for the electronic, the vibrational, and the electron–vibration interaction Hamiltonian, respectively. The electronic Hamiltonian $\hat{H}_{\mathrm{el}}$ includes LE and CT states. For the aggregation system, it reads

$$\begin{aligned}\hat{H}_{\mathrm{el}} = &\sum_{nmi} E_{n,m;L_i}|n,m;L_i\rangle\langle n,m;L_i| \\ &+ \sum_{nmi}\sum_{n'm'i'}{}' V_{nm,n'm';L_iL_{i'}}|n,m;L_i\rangle\langle n',m';L_{i'}|\end{aligned} \tag{2}$$

The diabatic state $|n,m;L_i\rangle$ corresponds to the n-th and m-th monomers being in the cationic and anionic states respectively if $m \neq n$; and for $m = n$, it corresponds to the n-th monomer being in the excited state. The index L_i is used to distinguish the electronic states with the same charge and excitation distribution. The diagonal element $E_{n,m;L_i}$ is the excitation energy, and $V_{nm,n'm';L_iL_{i'}}$ represents the electronic coupling between two states $|n,m;L_i\rangle$ and $|n',m';L_{i'}\rangle$.

For a donor–acceptor (D–A) system, the molecular vibrational Hamiltonian consists of contributions from both the donor and acceptor parts:

$$\hat{H}_{\mathrm{ph}} = \sum_n \sum_j \omega_{nj}\left(\hat{b}_{nj}^{\dagger}\hat{b}_{nj} + \frac{1}{2}\right), \tag{3}$$

where $\hat{b}_{nj}^{\dagger}$ and $\hat{b}_{nj}$ are the corresponding creation and annihilation operators of j-th vibrational mode in the n-th molecular fragment (which can be ZnPc or F_8ZnPc) with the frequency of ω_{nj}, respectively.

The electron–phonon interaction is used to describe the interaction between the different kinds of electronic states and the normal modes in a linear form

$$\hat{H}_{\text{el-ph}} = \sum_n \sum_j \omega_{nj}(\hat{b}_{nj}^{\dagger} + \hat{b}_{nj}) \otimes \hat{x}_{nj}, \tag{4}$$

with

$$\hat{x}_{nj} = \sum_{i,m} g_{nm,j;L_i}|n,m;L_i\rangle\langle n,m;L_i|. \tag{5}$$

The $g_{nm,j;L_i}$ is electron–phonon interaction parameter associated with the excited, cationic and anionic states, respectively. Here, we have assumed that the CT states with the same charge distribution share the same set of electron–phonon interaction constants.

Various numerical approaches for the calculations of electron–phonon interactions have been reported [43–45]. Here, we adopt the vertical gradient approximation, and the $g_{nj;L_i}$ factor is calculated by

$$g_{nj;L_i} = \sqrt{\frac{1}{2{\omega_{nj}}^3}}\frac{\mathrm{d}E_{nj;L_i}}{\mathrm{d}Q_{nj}}, \tag{6}$$

where $E_{nj;L_i}$ is the potential energy of corresponding electronic states and Q_{nj} is the normal coordinate of the j-th ground state vibrational mode on the n-th monomer, respectively. The parameters $g_{nm,j;L_i}$ are obtained by calculating the energy gradients of the L_i-th neutral singlet excited state; The electron–phonon coupling of CT states $g_{nm,j;L_i}$ includes the energy gradients of the n-th cationic monomer and the m-th anionic monomer. In the vertical gradient approximation, it is assumed that the frequency and coordinate direction of each normal mode are the same in all electronic states. This approximation is reasonable for most of organic molecules [38, 46].

B. Parameterization of the model Hamiltonian

Before performing quantum dynamics simulations, it is necessary to determine all the electronic structure parameters in Eqs. (2)–(6). These parameters include state energies and electronic couplings among LE and CT states, vibrational frequencies of normal modes, electron–phonon interaction parameters, and transition

DOI: 10.1063/1674-0068/cjcp2506086

dipole moments of donor and acceptor molecules. In a D–A system, CT states at the interface are also involved.

For the electronic part, traditional electronic structure theories are typically based on the adiabatic representation. In this case, appropriate diabatization methods are required to obtain quasi-diabatic states via adiabatic-to-diabatic (ATD) unitary transformations. In this work, we choose an eight-molecule model of the ZnPc–F_8ZnPc aggregate, comprising four ZnPc and four F_8ZnPc molecules. This model captures various quasi-diabatic states as well as short-range and long-range interactions. We employ the fragment particle-hole densities (FPHD) approach [47] to construct quasi-diabatic states, which is suitable for systems with multiple charge or excitation centers. In the FPHD approach, the optimal ATD unitary transformation matrix is determined by maximizing the localization of particle and hole densities on the predefined molecular fragments. Based on the resulting distributions of particle and hole densities, LE and CT states can be readily identified in both donor and acceptor systems. The input for FPHD calculations includes the energies and transition density matrices of adiabatic excited states, which are routinely obtained from TD-DFT calculations. In the FPHD calculation, all adiabatic states below a predefined energy threshold are included without artificial selection, and we have verified that this threshold is sufficiently high to ensure converged results. For further details on the rationale and implementation of the FPHD scheme, readers are referred to Refs. [41, 47].

C. Non-Markovian stochastic Schrödinger equation

Based on the constructed model Hamiltonian of the aggregate, photophysical process can be simulated using the NMSSE [42]

$$i\frac{\partial}{\partial t}|\psi_\xi(t)\rangle = \Big[\hat{H}_{\rm el} + \sum_{nj}\xi_{nj}(t)\hat{x}_{nj} - i\sum_{nj}\hat{x}_{nj}\int_0^t \hat{x}_{nj}(-\tau)\alpha_{nj}^{\rm res}(\tau){\rm d}\tau\Big]|\psi_\xi(t)\rangle, \tag{7}$$

where $|\psi_\xi(t)\rangle$ is the stochastic wavefunction, $\xi_{nj}(t)$ is the phonon-induced time-dependent stochastic fields, satisfying $\hat{x}_{nj}(t) \equiv {\rm e}^{i\hat{H}_{\rm el}t}\hat{x}_{nj}{\rm e}^{-i\hat{H}_{\rm el}t}$, and the expression of the residual correlation functions is

$$\alpha_{nj}^{\rm res}(t) = \tanh\left(\frac{\beta\omega_{nj}}{4}\right)\cos(\omega_{nj}t) - i\sin(\omega_{nj}t). \tag{8}$$

These random fields can be generated via the following expressions:

$$\xi_{nj}(t) = \sqrt{\frac{\overline{n}_{nj}+1}{2}}(\gamma_{nj}^1 + i\gamma_{nj}^2){\rm e}^{i\omega_{nj}t} + \sqrt{\frac{\overline{n}_{nj}}{2}}(\gamma_{nj}^1 - i\gamma_{nj}^2){\rm e}^{-i\omega_{nj}t}, \tag{9}$$

where $\bar{n}_{nj} \equiv 1/({\rm e}^{\beta\omega_{nj}}-1)$, and γ_{nj}^1 and γ_{nj}^2 are independent Gaussian white noises satisfying $\langle\gamma_{nj}^i\rangle = 0$ and $\langle\gamma_{nj}^i\gamma_{n'j'}^{i'}\rangle = \delta_{nn'}\delta_{jj'}\delta_{ii'}$.

In the framework of the NMSSE, the impact of the vibronic effect on dynamics processes is incorporated through phonon-induced stochastic fields and non-Markovian term. Typically, researchers are more interested in the system's internal evolution trajectory. Consequently, it is feasible to eliminate the environmental degrees of freedom and concentrate on the dynamics of the reduced density matrix for the electronic subsystem. This reduced density matrix is given by:

$$\hat{\rho}_{\rm el}(t) = {\rm Tr}_{\rm ph}\left\{{\rm e}^{i\hat{H}t}|\psi_0\rangle\langle\psi_0|\frac{{\rm e}^{-\beta\hat{H}_{\rm ph}}}{Z_{\rm ph}}{\rm e}^{-i\hat{H}t}\right\}, \tag{10}$$

where $Z_{\rm ph} \equiv {\rm Tr}\{{\rm e}^{-\beta\hat{H}_{\rm ph}}\}$, $|\psi_0\rangle$ denotes the initial state vector, and ${\rm Tr}_{\rm ph}$ represents the trace operation over all phononic degrees of freedom. Under the initial condition $|\psi_\xi(0)\rangle = |\psi_0\rangle$, using standard algorithms such as the fourth-order Runge–Kutta method, Eq.(7) can be solved to obtain the time-dependent wavefunction $|\psi_\xi(t)\rangle$. The molecular vibrations are assumed to satisfy the thermal equilibrium distribution at the beginning of dynamics evolution. The reduced density matrix of the electronic degrees of freedom is obtained by averaging over all random wavefunctions, that is:

$$\hat{\rho}_{\rm el}(t) = M\left[|\psi_\xi(t)\rangle\langle\psi_\xi(t)|\right]_\xi, \tag{11}$$

where $M[\cdot]_\xi$ represents the average over the random fields. The vibrationally-resolved absorption spectra of the aggregate can be obtained using the linear response theory. The detailed implementation [37–39] of Eq.(7) for the calculations of absorption spectra and quantum dynamics can be found in Ref.[48].

D. Computational details

We utilize the structure of copper phthalocyanine

DOI: 10.1063/1674-0068/cjcp2506086

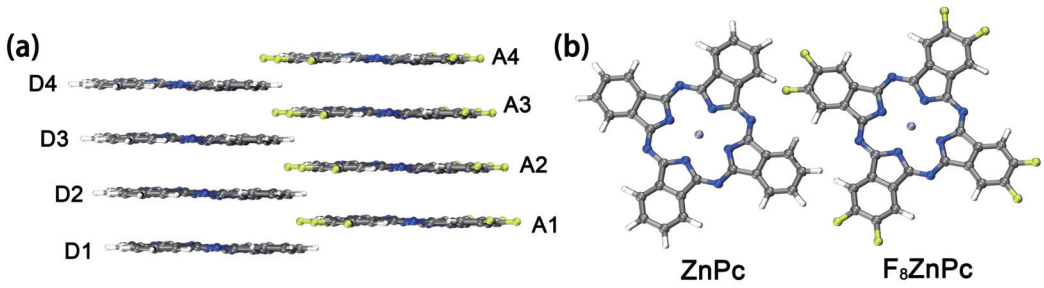

FIG. 1 (a) Side view of the optimized geometry of ZnPc–F_8ZnPc, (b) top view of the optimized geometry of ZnPc–F_8ZnPc. D1–D4 represent the 1st–4th ZnPc donor molecules and A1–A4 represent the 1st–4th F_8ZnPc acceptor molecules.

(CuPc) [49] as the initial configuration. Subsequently, Cu atoms are replaced by Zn atoms and hydrogen atoms are selectively replaced by fluorine atoms while keeping other atoms unchanged. Based on density functional theory, geometry optimization is carried out using the Perdew–Burke–Ernzerhof (PBE) functional [50] within the VASP software package [51]. The PAW pseudopotential is employed, with a plane-wave cutoff energy of 520 eV. A Γ-centered k-point mesh of $2\times6\times2$ is used, and the energy and force convergence criteria of geometry optimization are set to 10^{-6} eV and 0.01 eV/Å, respectively. Based on the obtained donor–acceptor heterostructure, we select ZnPc–F_8ZnPc aggregate consisting of four ZnPc molecules and four ZnPc molecules as the model system. Tamm–Dancoff approximation (TDA) of TDDFT are performed to calculate the adiabatic states of the octamer using the range-separated functional CAM-B3LYP [52] and def2-SVP [53] basis set, and in combination with the SMD solvent model (the dielectric constant is set to 5.0 to simulate the surrounding crystal environment). The vibrational frequencies and relative energy gradients of ZnPc and F_8ZnPc monomers are calculated at B3LYP [54]/def2-SVP level of theory. All quantum chemical calculations of monomers and octamer are performed using the Gaussian 16 software package [55].

The diabatic states and their electronic couplings are calculated based on the adiabatic states using our in-house FPHD code. And the electron and hole distributions of diabatic states are generated and visualized by Multiwfn 3.8 [56] and VMD 1.9.3 [57] software. The vibrational-resolved absorption spectra and exciton dynamics of the ZnPc–F_8ZnPc system are simulated using our implementation of NMSSE, where all vibrational modes are included. Generally, the temperature is set at 300 K, the adopted time step is 0.4 fs. The wavefunctions of all trajectories remain normalized during the simulation to ensure the correct convergence of the dynamics.

III. RESULTS AND DISCUSSION

A. Diabatic states and their couplings

The ZnPc–F_8ZnPc aggregate with an edge-on stacking configuration, which consists of four ZnPc molecules (D1–D4) and four F_8ZnPc molecules (A1–A4), is illustrated in FIG. 1. The diabatic states and their couplings obtained by FPHD diabatization scheme for ZnPc–F_8ZnPc aggregate are visualized in FIGs. 2, 3, and 4. FIG. 2 presents the exciton energy transfer process within the ZnPc, F_8ZnPc system and at the ZnPc–F_8ZnPc interface as well as the energies of the individual LE states. As can be seen from the figure, the LE energies of ZnPc molecules at the center and boundary positions are 2.07 eV and 2.04 eV, respectively, and LE energies of F_8ZnPc molecules at the center and boundary positions are 2.09 eV and 2.06 eV, respectively. The LE state energies of ZnPc–F_8ZnPc molecules are dependent on their position, with the energies of the edge molecules being slightly lower than those at the center, by approximately 0.03 eV. Additionally, the LE state energy of ZnPc is slightly lower than that of F_8ZnPc, by about 0.02 eV. In both the ZnPc and F_8ZnPc systems, the exciton coupling values for the nearest neighbors, next-nearest neighbors, and third-nearest neighbors are on similar orders of magnitude, being approximately 100 meV, 17 meV, 5 meV, and 100 meV, 14 meV, 4 meV, respectively. This demonstrates that the LE state energies of ZnPc and F_8ZnPc molecules are similar, and that there are analogous energy transfer processes within the molecules. The above results confirm that the substitution of fluorine atoms has little impact on the excited state properties of the ZnPc aggregate. It is noteworthy that the nearest excitonic coupling value (14 meV) between ZnPc and F_8ZnPc molecules at the interface is reduced compared to the excitonic coupling values within the individual ZnPc

DOI: 10.1063/1674-0068/cjcp2506086

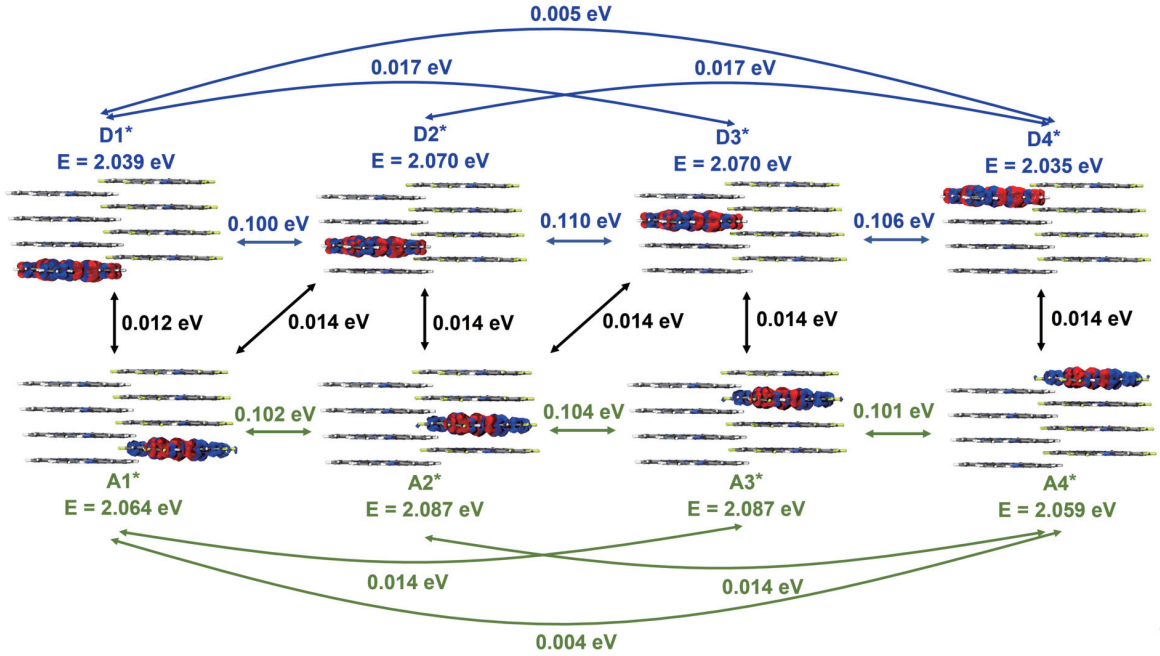

FIG. 2 The LE–LE coupling values and the energies of LE states in ZnPc–F_8ZnPc calculated via FPHD. The blue, green, and black arrows represent the energy transfer processes within ZnPc, F_8ZnPc molecules, and at the ZnPc–F_8ZnPc interface, respectively. The excitonic couplings between the two LE states are shown in the same colors next to the arrows. The blue and red isosurfaces with an isovalue of 0.0005 a.u. present the hole and electron density distributions, respectively. The excited monomer in the aggregate is denoted by the superscript '*'.

and F_8ZnPc systems. Compared to the face-on configuration, the spatial arrangement and orientation at the interface results in smaller coupling values because the distance between the transition dipoles on donor and acceptor at the interface are larger when molecules are stacked in an edge-on orientation. This indicates that after molecular excitation, energy tends to be transferred to neighboring molecules of the same type.

FIG. 3 represents the processes of hole and electron transfer within ZnPc and F_8ZnPc molecules as well as at the D–A interface. Note that the LE states have the highest energy, intramolecular CT states have lower energy, and interfacial CT states have the lowest energy. Both the intramolecular CT states and interfacial CT states have lower energies than the LE states. The molecules tend to transform from high-energy LE states to low-energy CT states after excitation. In addition, in ZnPc and F_8ZnPc molecules, the electron transfer integrals (about 0.1 eV) are much larger than the hole transfer integrals (about 0.01 eV). This indicates that within these molecules, the LE states tend to dissociate mainly through electron transfer. Since the energies of the LE states and the intramolecular charge transfer states are very close and there is a large coupling value between them, the LE states and the charge transfer states are easily mixed and show the characteristics of the mixed state. This has been verified in the subsequent spectral simulations. Since the coupling values of the LE and intramolecular CT states are much larger than those of the interfacial CT states, it indicates that the excitons tend to dissociate within the molecule first to form intramolecular CT states. Meanwhile, the lowest energy of CS state within the pure molecules we calculate is 2.41 eV, which indicates that the intramolecular CT states have difficulty transforming into the high-energy intramolecular CS states, they will gradually evolve into the interfacial CT states.

After the formation of the interfacial CT state, electrons are transferred to the acceptor F_8ZnPc, while holes are transferred to the donor ZnPc. To investigate the subsequent transfer processes of electrons and holes within the acceptor and donor, we consider two cases. In the first case, we analyze the electron transfer within the acceptor F_8ZnPc with the hole being localized on D2 molecule; while in the second case, the hole transfer within the donor ZnPc is studied with electron being fixed on the A3 molecule. The results related to the electron transfer pathway within the acceptor are shown in the upper part of FIG. 4. The coupling value between adjacent electron transfer states in F_8ZnPc is

DOI: 10.1063/1674-0068/cjcp2506086

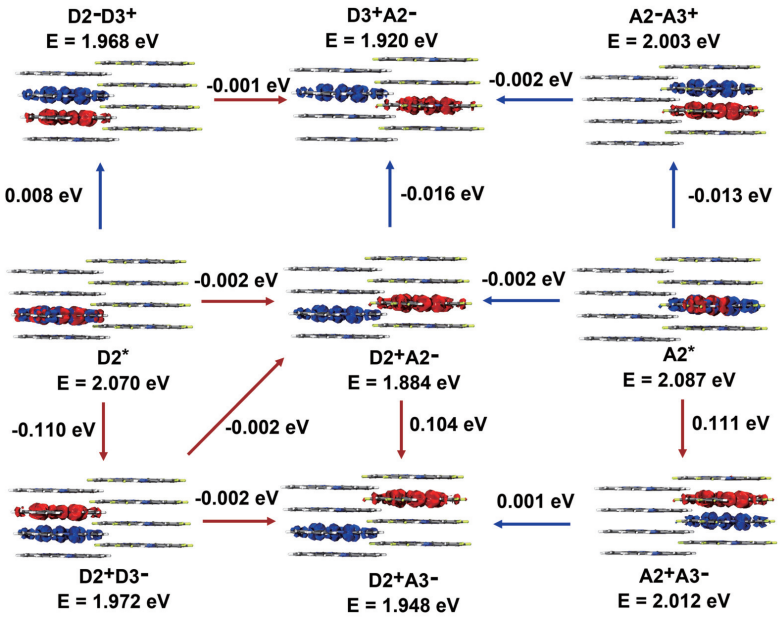

FIG. 3 The process of exciton dissociation, hole and electron transfer in the ZnPc–F_8ZnPc system. The blue arrows correspond to hole transfer and the red arrows to electron transfer. The numbers next to the arrows are the values of the coupling between the two states. Superscript '*' denotes the excited state and the superscript '–' and '+' denote the charged states. For example, D2* indicates that the second donor molecule ZnPc is in excited state, $D2^-D3^+$ indicates that the D2 molecule is in the anionic state and the D3 molecule is in the cationic state.

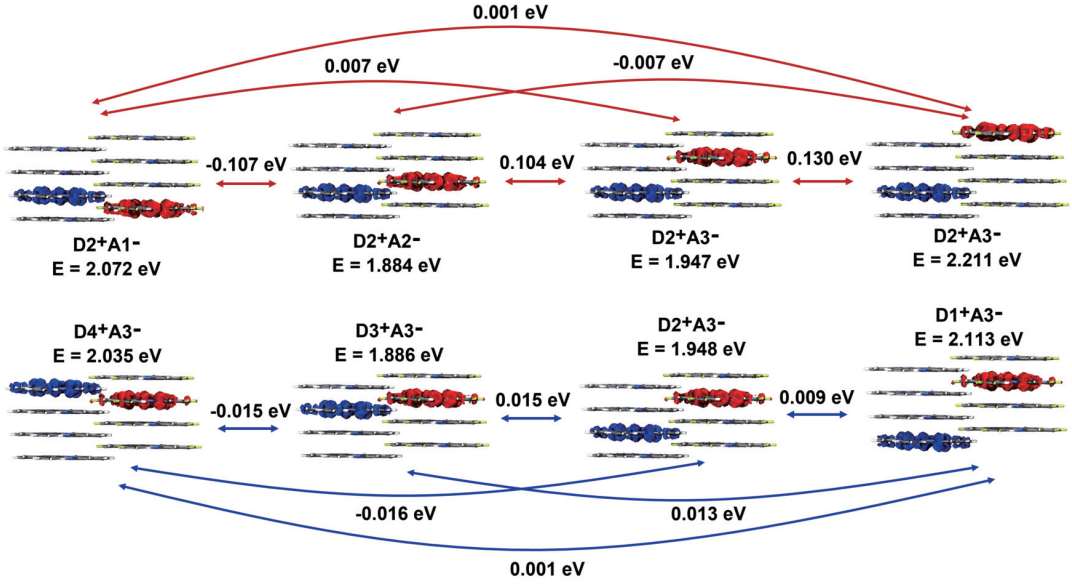

FIG. 4 The electron transfer process within F_8ZnPc (upper) and the hole transfer process within ZnPc (lower), respectively.

approximately 100 meV, while the coupling value for next-nearest neighbors is 7 meV. The larger coupling value allows electrons to jump easily between the adjacent F_8ZnPc molecule, thus achieving efficient electron transport within the F_8ZnPc molecular chain. The results of hole transfer pathway within the donor are visualized in the lower part of FIG. 4. The coupling value between adjacent hole transfer processes in ZnPc is about 15 meV. However, an unexpectedly larger value appears for the next-nearest neighbor hole transfer integral (the coupling value between $D4^+A3^-$ and $D2^+A3^-$ is 16 meV). The same trend occurs when the electron is localized on other acceptor molecules while holes are transferred within donor molecules. We speculate that this unusual behavior is due to the Coulomb interaction between electron and hole. As the hole is

DOI: 10.1063/1674-0068/cjcp2506086

farther away from the electron, the Coulomb attraction becomes weaker so that it is easier for the hole to jump away from the electron. This phenomenon does not occur for electron transfer in the acceptor, and we speculate that it is due to the large coupling value between neighboring electron transfer processes and the fact that the Coulomb force is not dominant in this case.

B. Absorption spectra of ZnPc–F_8ZnPc aggregates

The pure-electronic absorption spectra and vibrationally resolved absorption spectra of the ZnPc–F_8ZnPc octamer are plotted in FIG. 5. The pure-electronic spectra are obtained from the TDA calculation using a Gaussian broadening function with a half width at half maximum (HWHM) of 0.07 eV. To better match the experimental result [16], all calculated spectra are redshifted by 0.2 eV. In addition, we have normalized the peak intensities of all calculated spectra for a direct comparison of the spectral shapes and the positions. After the shift, the first and second peaks of the theoretically simulated vibrationally resolved absorption spectra are 1.53 eV and 1.74 eV, respectively, with a peak interval of 0.2 eV. The experimental values are 1.53 eV and 1.73 eV. The theoretical simulation results are highly consistent with the experimental data [16]. The above results show that the model Hamiltonian we construct is reasonable and can be used for subsequent dynamics simulations.

As can be seen from the FIG. 5, the intensity of the high-energy absorption peak is always higher than that of the low-energy absorption peak. To further analyze the nature of the electronic states that play an important role in the spectral features, we have calculated the proportions of the LE states and CT states in the adiabatic excited states in different energy regions, as shown in Table I. We find that the characteristic absorption peaks in both the low-energy and high-energy regions are contributed by the mixing of LE and CT states. The low-energy excited states (S_1, S_9) with smaller oscillator strengths are mainly contributed by the interfacial CT states. The intermediate excited states (S_{18}, S_{32}) with larger oscillator strengths are mainly contributed by the LE states and CT states within the ZnPc molecules. The high-energy excited states (S_{66}, S_{67}) with the largest oscillator strengths are jointly contributed by the LE states and CT states within both ZnPc and F_8ZnPc molecules.

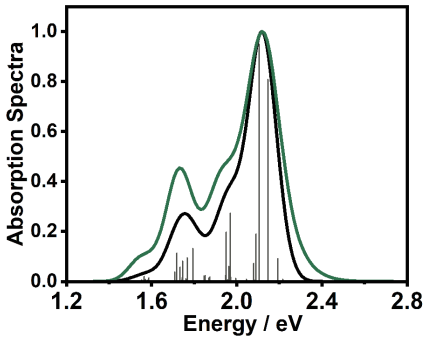

FIG. 5 Theoretically simulated UV-visible absorption spectra (black line) and vibrationally resolved absorption spectra (green line) of the ZnPc–F_8ZnPc octamer. The gray vertical lines represent the oscillator strengths of adiabatic states.

TABLE I The components of LE and CT states in the low-lying adiabatic excited states with excitation energy E (in eV) for 4D–4A systems.

Adiabatic state	ZnPc		F_8ZnPc		Interfacial
(E)	LE	CT	LE	CT	CT
S_1 (1.70)	0.001	0.001	0.000	0.000	0.998
S_9 (1.76)	0.001	0.003	0.021	0.038	0.937
S_{18} (1.93)	0.340	0.633	0.002	0.004	0.021
S_{32} (2.00)	0.203	0.786	0.003	0.007	0.001
S_{66} (2.31)	0.574	0.117	0.146	0.160	0.002
S_{67} (2.36)	0.212	0.032	0.533	0.214	0.009

C. Photo-induced dynamics processes in the aggregates

Next, we will use the NMSSE method to further investigate the photo-induced exciton dynamics in ZnPc–F_8ZnPc aggregates. The discussion focuses on the factors that affect the charge separation mechanism in this aggregate system. In the dynamics simulation, the 70 electronic states with the lowest energies in the octamer are selected. Meanwhile, each ZnPc and F_8ZnPc molecule contains 165 localized vibrational modes, and the dynamics process includes all vibrational modes of the eight molecules, which amounts to a total of 1320 vibrational modes. The relative energy between the LE states and CT states remains constant, the simulation results will be consistent regardless of whether the energy data have been shifted. Therefore, in dynamics simulations, we utilize the original energy data without shifting.

1. Photo-physics processes with different initial states

Firstly, we explore the impact of the initial excitation energy on the dynamics of the ZnPc–F_8ZnPc aggregate. We select three different energy windows of

DOI: 10.1063/1674-0068/cjcp2506086

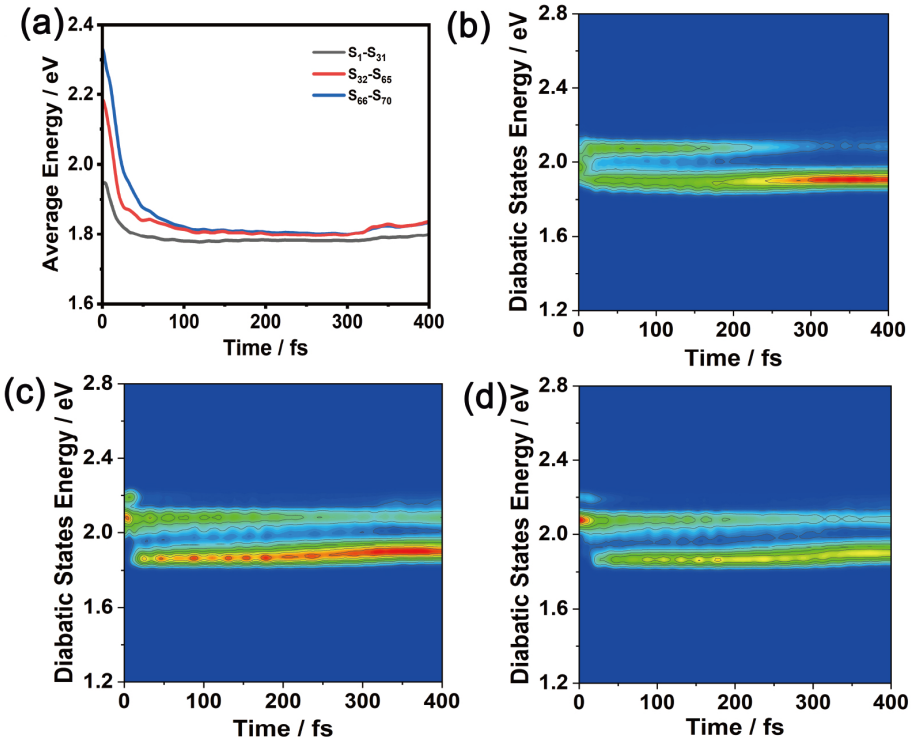

FIG. 6 (a) Time evolution of the average electronic energy under three different initial states (S_1–S_{31}, S_{32}–S_{65}, and S_{66}–S_{70}). Time evolution of the energy-resolved distribution of diabatic states under three different initial excited states (b) S_1–S_{31}, (c) S_{32}–S_{65}, and (d) S_{66}–S_{70}.

adiabatic states as the initial conditions for dynamical evolution, which include S_1–S_{31} (1.70–1.98 eV), S_{32}–S_{65} (2.00–2.30 eV), and S_{66}–S_{70} (2.31–2.43 eV). The weights (percentages) of the adiabatic states in a given energy window are determined by the relative magnitude of their oscillator strengths.

The evolution of the average energy expectation and the diabatic state population of ZnPc–F_8ZnPc aggregate under three different initial conditions are shown in FIG. 6. The average electronic energy of the aggregate is calculated using the formula $\bar{E}(t) = \mathrm{Tr}\{\hat{H}_{\mathrm{el}}\hat{\rho}_{\mathrm{el}}(t)\}$, where $\hat{\rho}_{\mathrm{el}}(t)$ is the reduced density matrix in the electronic degree of freedom. From FIG. 6(a), it can be seen that under the three different initial conditions, the system rapidly relaxes from the high-energy initial states to lower energy states with different rates during 100 fs. After 100 fs, the vibronic coupling between the electronic states and the molecular vibrations maintains the system in quasi-stationary states. The average energy of the low-energy initial states S_1–S_{31} being approximately 1.78 eV, while the average energies of S_{32}–S_{65} and S_{66}–S_{70} are about 1.81 eV. In our previous study, the face-on stacked ZnPc–F_8ZnPc system had a similar average energy dynamics evolution process [33].

The energy-resolved population of diabatic states is determined by the following expression

$$P(E,t) = \frac{1}{\sigma\sqrt{2\pi}} \sum_n \rho_{n,n}(t) \mathrm{e}^{-\frac{(E-E_n)^2}{2\sigma^2}},$$

where E_n and $\rho_{n,n}(t)$ represent the energy and population of the diabatic state n. The population evolution of diabatic states under the initial conditions S_1–S_{31}, S_{32}–S_{65}, and S_{66}–S_{70} are plotted in FIG. 6 (b), (c), and (d) respectively, in which the blue color indicates a low occupancy, while red color represents the high occupancy. From FIG. 6(b), it can be seen that the system mainly occupies high-energy diabatic states initially. After 250 fs, the high-energy states almost disappear, evolving into low-energy CT states. FIG. 6 (c) and (d) indicate that the population of high-energy diabatic states will gradually decrease but will not completely disappear throughout the entire dynamics process under these high-energy initial condition. The above analysis shows that, in the dynamics evolution under three different initial conditions, the excitons all tend to transform from high-energy LE states to low-energy CT states. This conclusion is consistent with our previous dynamics results on face-on stacked ZnPc–F_8ZnPc

DOI: 10.1063/1674-0068/cjcp2506086

polymers.

FIG. 6 only presents the time evolution of energy distribution of the ZnPc–F_8ZnPc system. To see the process of exciton dissociation, we plot the population evolution of LE states, the intramolecular CT states, and the interfacial CT states in FIG. 7 under different initial conditions. From FIG. 7 (a) and (b), it is evident that the population of the interfacial CT states (CT-Inter) begins to increase significantly after approximately 50 fs. In contrast, the increase in the interfacial CT states population shown in FIG. 7(c) starts slightly later at around 100 fs. This is because the initial populations of the diabatic states are different for the three initial states. In initial conditions S_1–S_{31} and S_{32}–S_{65}, the initial population of the intramolecular CT states (CT-Intra) is greater than that of LE states. Compared to the exciton dissociation into interfacial CT states, the electron/hole of intramolecular CT states jump to form interfacial CT states more rapidly. Because of the strong coupling and quantum coherence between the LE state and the intramolecular CT state, the LE states delocalized on the molecules will first dissociate simultaneously into intramolecular CT states. This leads to the generation of intramolecular CT states is more rapidly than interfacial CT states at the beginning. Additionally, the population dynamics in FIG. 7 show an oscillatory pattern with a period of approximately 22 fs. Our simulations show that there are large recombination energies with respect to the stretching vibrations in the C–C and C–N bonds. This shows that the population oscillations are due to the vibronic coupling between the electronic states and the molecular vibrations. It is worth noting that the oscillation between the LE states and the intramolecular CT states is particularly significant in the first 200 fs of the dynamics. This indicates that the vibronic coupling effect maintains a certain dynamical equilibrium distribution between the LE states and the intramolecular CT states, which prevents the direct generation of interfacial CT states. In all cases, after 350 fs, the populations of the interfacial CT states show a decreasing trend, while the populations of LE states and the intramolecular CT states increase. This is because the finite length of the aggregates limits the further outward movement of electron and hole, and long-time dynamics simulation will lead to oscillations in the populations of the diabatic states.

Dynamics simulations are also performed without considering vibration effects (*i.e.*, making the electron-phonon coupling zero), and relevant results including

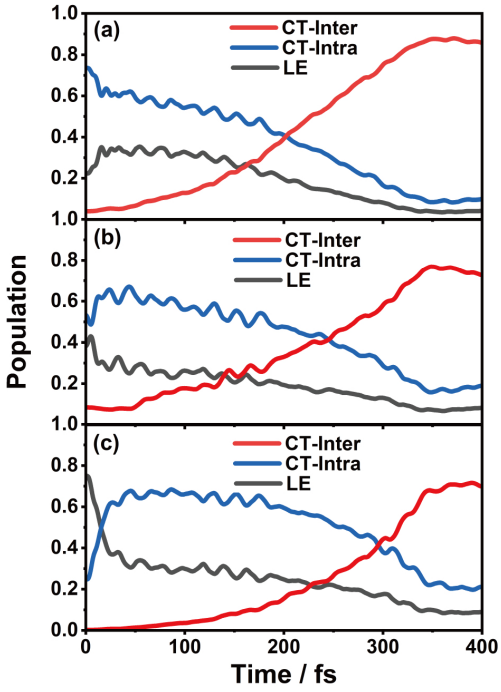

FIG. 7 Under three different initial states (a) S_1–S_{31}, (b) S_{32}–S_{65}, and (c) S_{66}–S_{70}, the population evolution of the various quasi-diabatic states including LE, CT-Intra (intramolecular CT states), and CT-Inter (interfacial CT states).

average energy, energy-resolved population of diabatic states, and population evolution of diabatic states are shown in the FIG. S1 of Supplementary materials (SM). In this case, the evolution of average energy remains unchanged. The energy-resolved distribution of diabatic states and the populations of LE and intramolecular CT states maintain an oscillatory pattern, while the population of the interfacial CT state does not increase.

The above results show that at three different initial excitation energies, although the dynamic evolution process is similar (LE and intramolecular CT states gradually evolve into interfacial CT states). However, the time scales for the generation of interfacial CT states are different. The vibronic coupling allows the system to relax from higher energy states to lower energy states, maintaining the quasi-stationary states for a period of time. This allows the LE states to evolve into intramolecular CT states, but prevents the rapid generation of interfacial CT states.

To investigate the specific impacts of exciting donor and acceptor molecules on the dynamics processes, we consider the cases where only the donor molecules and only the acceptor molecules are excited, respectively. As can be seen in FIG. 8(a), after the excitation of ZnPc molecule, the exciton rapidly dissociates on the ZnPc

DOI: 10.1063/1674-0068/cjcp2506086

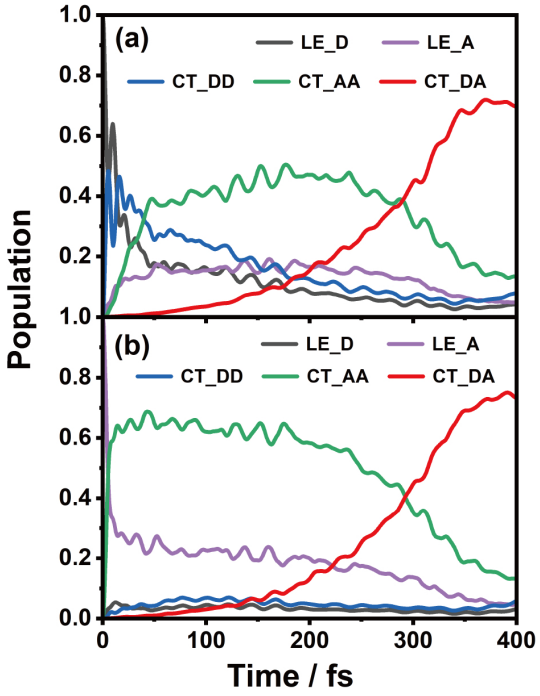

FIG. 8 Population evolution of various LE states and CT states in the in ZnPc–F_8ZnPc system under two different initial states: (a) ZnPc molecular excitation and (b) F_8ZnPc molecular excitation. CT_DD and CT_AA represent the intramolecular charge separated states of ZnPc and F_8ZnPc, respectively. CT_DA represents the interfacial charge separated states.

molecules, causing the increase in CT_DD population. At the same time, this process is accompanied by obvious energy transfer to the donor F_8ZnPc molecule, which is indicated by the increase in the CT_DD population. The population of CT state is larger than that of the LE state within the F_8ZnPc molecules, suggesting a more efficient electron transfer process ($D^+D^- \rightarrow D^+A^-$) at the D–A interface. When the F_8ZnPc molecules are excited, as shown in FIG. 8(b), the energy transfer from acceptor to donor is inefficient so that LE_D population remains nearly constant. In contrast, the exciton will rapidly dissociate on the F_8ZnPc molecules which is suggested by the rapid rise in CT_AA population, followed by hole transfer across the interface to form interfacial CT states ($A^-A^+ \rightarrow A^-D^+$). Although excitation of different molecules leads to distinct dynamics evolutions, the generation timescales of the interface CT states and the final population are similar.

2. Temperature and coherence effects in dynamics processes

To investigate the temperature effect and the coherence effect on the dynamics, we perform NMSSE simulations at different temperatures and also consider the case without electron–phonon interaction. The two adiabatic states with the largest oscillator strength are chosen as the initial state. The corresponding coherence participation ratio (CPR) of the CT states as well as their population evolution from the dynamics simulations are plotted in FIG. 9 (a) and (b). CPR measures the degree of coherence [58–60] and is expressed as

$$\mathrm{CPR}(t) = \frac{\left(\sum_{n_i n_j} \left|\langle n_i|\hat{\rho}_{\mathrm{el}}(t)|n_j\rangle\right|\right)^2}{\mathrm{PPR}(t)\sum_{n_i n_j}\left|\langle n_i|\hat{\rho}_{\mathrm{el}}(t)|n_j\rangle\right|^2}, \tag{12}$$

where the population participation ratio (PPR) is defined as

$$\mathrm{PPR}(t) = \frac{\left(\sum_{n} \mathrm{Pop}(t)\right)^2}{\sum_{n}\left|\langle n|\hat{\rho}_{\mathrm{el}}(t)|n\rangle\right|^2}. \tag{13}$$

Here, the index n labels the diabatic state, and $\mathrm{Pop(t)} = \langle n|\rho|n\rangle$ represents the diabatic state population. In the absence of electron–phonon interaction (marked as 'No-e-ph'), the CPR remains oscillatory, indicating that a certain degree of quantum coherence still exists in the system without the influence of phonons. This oscillation (coherence) is due to the electronic coupling between the inherent CT states at the initial time. When electron–phonon coupling is included, the CPR rapidly decreases from a high initial value (around 18) to a lower value (around 6), which is due to the loss of quantum coherence caused by the electron–phonon interaction. There is little difference in the CPR evolution between 200 K and 300 K, indicating that the low temperature has less effect on the CPR. This is because the thermal rise and fall of the system is smaller at low temperatures, allowing quantum coherence to be better preserved. In contrast, the CPR slightly increases (between 270–320 fs) at 300 K, which may be due to the increasing number of phonons at high temperatures. The stronger electron–phonon interaction promotes the generation of interfacial CT states, and the rapid transition between diabatic states leads to the increase of quantum coherence.

FIG. 9(b) shows the population evolution of interfacial CT states at different temperatures, while the pop-

DOI: 10.1063/1674-0068/cjcp2506086

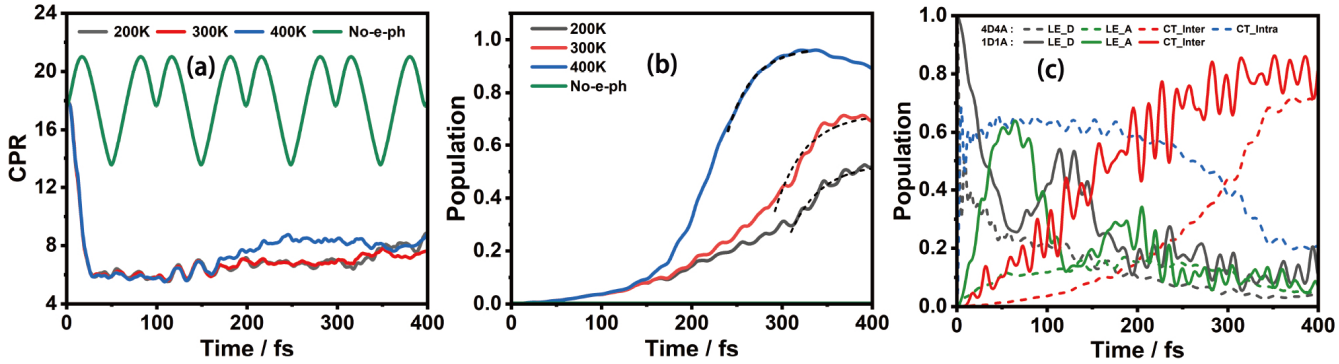

FIG. 9 (a) The coherence participation ratio of CT states at different temperatures and without electron–phonon interaction. (b) The population evolution of interfacial CT states. (c) The population evolution of diabatic states at different aggregate lengths. LE_D and LE_A represent the locally excited states of ZnPc and F_8ZnPc, respectively. The dashed lines and solid lines represent the 4D4A and 1D1A aggregates, respectively. The simulated 1D1A system is placed in aggregated environment.

ulation evolution of all diabatic states is shown in FIG. S2 of SM. It can be seen that in the absence of vibronic coupling effect, there is almost no additional generation of interfacial CT states (the green line is almost invisible in the figure). At first, the main process is the dissociation of excitons to form intramolecular CT states, and only a small amount of interfacial CT states are generated by exciton dissociation at any temperature. Then, the generation of interfacial CT states is contributed by intramolecular CT states. As time evolves, the quantum coherence between CT states decreases, allowing intramolecular CT states to rapidly evolve into interfacial CT states. In the late stage of the dynamics, the population of interfacial CT states shows an exponential growth trend, so we speculate that the transport of electrons or holes at this time is a hopping process. In order to determine the formation rate of the interfacial CT states, we adopt the function $y = y_0 + A\exp\left(-\dfrac{t-t_0}{\tau}\right)$ to fit the population evolution curves at different temperatures, where τ is the time constant, and $K = \tau^{-1}$ is the rate constant. The fitted values of K at temperature of 200, 300, and 400 K are 2.9×10^{13}, 3.0×10^{13}, and 3.5×10^{13} s^{-1} respectively (more detailed results of fitting can be found in the Table S1 of SM). The results show that with the increase of temperature, the population of the interfacial CT states increase faster and finally reaches a higher population value.

In FIG. 9(c), we simulate evolution of the population with different aggregate lengths. The 1D1A aggregate (one donor molecule and one acceptor molecule) corresponds to the D2 and A2 fragments in the 4D4A aggregate, and the electronic structure parameters of 1D1A are also the same as those of the D2 and A2 fragments. In 1D1A system, the electronically excited donor molecule is set as the initial condition, while in 4D4A aggregate, only D2 molecule is initially excited. It can be seen that the 1D1A aggregate exhibits significant energy exchange and rapidly forms CT states at the very beginning. The population of interfacial CT states in the 1D1A aggregate increases more quickly than that in the 4D4A aggregate, which is due to the fact that excitons in the 4D4A aggregate initially dissociate into intramolecular CT states. In addition, the population changes in the 1D1A aggregate are more dramatic, which may indicate that the conversion between LE and CT states is more likely to occur in shorter aggregates due to higher quantum coherence.

IV. CONCLUSION AND OUTLOOK

In this paper, we have simulated the excited-state properties, vibrationally resolved absorption spectra, and exciton dynamics of the edge-on stacked ZnPc–F_8ZnPc octamer using first-principles calculations. The theoretically simulated absorption spectrum of the aggregate is in good agreement with the experimental data, validating the rationality of the constructed Hamiltonian. Using the non-Markovian stochastic Schrödinger equation, we simulate the ultrafast dynamics of the aggregate and explore the effects of several contentious factors on the dynamics process. The results show that the time scales for generating interfacial CT states with different initial excitation energies are slightly different. Low-energy initial excited states can generate interfacial CT states more quickly. The vibronic coupling effect causes the system to relax rapid-

DOI: 10.1063/1674-0068/cjcp2506086

ly from a high-energy excited state to a low-energy excited state and maintains quasi-stationary states for a period of time. The formation of quasi-stationary state allows the intramolecular LE states and CT states to maintain a steady-state oscillation for a period of time, hindering the direct generation of interfacial CT states. Compared with the dissociation of excitons into interfacial CT states, there is a faster rate of electrons/holes in intramolecular CT states jump to form interfacial CT states. Quantum coherence interactions cause a rapid oscillatory phenomenon in the populations of diabatic states within the 1D1A aggregate. We also simulate the effect of temperature on the generation rate of interfacial CT states. The results show that high temperature can promote the generation of interfacial CT states. The thermal effect allow for longer and faster hopping processes in aggregates. Through the dynamics simulation of the ZnPc–F_8ZnPc aggregate, we elucidate several factors affecting exciton dissociation, which provides important theoretical support for the design and optimization of high-performance organic photovoltaic devices.

Supplementary materials: The energy, population, and fitted parameter values, and the atomic coordinates of the ZnPc–F_8ZnPc octamer.

V. NOTES

The authors declare no competing financial interests.

VI. ACKNOWLEDGMENTS

This work is supported by the National Natural Science Foundation of China (Nos. 22033006, 22173074, 22473091, and 92372105).

[1] Y. Zhao and W. Liang, Chem. Soc. Rev. **41**, 1075 (2012).
[2] G. Zhang, F. R. Lin, F. Qi, T. Heumüller, A. Distler, H. J. Egelhaaf, N. Li, P. C. Y. Chow, C. J. Brabec, A. K. Y. Jen, and H. L. Yip, Chem. Rev. **122**, 14180 (2022).
[3] R. Sun, Y. Wu, X. Yang, Y. Gao, Z. Chen, K. Li, J. Qiao, T. Wang, J. Guo, C. Liu, and L. Zhang, Adv. Mater. **34**, 2110147 (2022).
[4] C. He, Y. Pan, Y. Ouyang, Q. Shen, Y. Gao, K. Yan, J. Fang, Y. Chen, C. Q. Ma, J. Min, and Z. Li, Energy Environ. Sci. **15**, 2537 (2022).
[5] L. Zhu, M. Zhang, J. Xu, C. Li, J. Yan, G. Zhou, W. Zhong, T. Hao, J. Song, X. Xue, and H. Wang, Nat. Mater. **21**, 656 (2022).
[6] J. Liu, Y. Shi, J. Dong, M. I. Nugraha, X. Qiu, M. Su, R. C. Chiechi, D. Baran, G. Portale, X. Guo, and L. J. A. Koster, ACS Energy Lett. **4**, 1556 (2019).
[7] L. Li, R. Sun, and R. Zheng, Mater. Des. **197**, 109209 (2021).
[8] L. Lüer, R. Wang, C. Liu, H. Dube, T. Heumüller, J. Hauch, and C. J. Brabec, Adv. Sci. **11**, 2305948 (2024).
[9] K. Nakamura, L. Guérin, G. Privault, K. Nakabayashi, M. Hervé, E. Collet, and S. I. Ohkoshi, Nat. Commun. **16**, 5012 (2025).
[10] P. Cheng, G. Li, X. Zhan, and Y. Yang, Nat. Photon. **12**, 131 (2018).
[11] G. Grancini, M. Maiuri, D. Fazzi, A. Petrozza, H. J. Egelhaaf, D. Brida, G. Cerullo, and G. Lanzani, Nat. Mater. **12**, 29 (2013).
[12] H. Tamura and I. Burghardt, J. Am. Chem. Soc. **135**, 16364 (2013).
[13] A. Y. Sosorev, D. Y. Godovsky, and D. Y. Paraschuk, Phys. Chem. Chem. Phys. **20**, 3658 (2018).
[14] L. Perdigón-Toro, H. Zhang, A. Markina, J. Yuan, S. M. Hosseini, C. M. Wolff, G. Zuo, M. Stolterfoht, Y. Zou, F. Gao, and X. Wang, Adv. Mater. **32**, 1906763 (2020).
[15] N. Zorn Morales, D. S. Rühl, E. List-Kratochvil, and S. Blumstengel, Phys. Status Solidi A **221**, 2300186 (2024).
[16] T. R. Kafle and W. L. Chan, Phys. Rev. Appl. **15**, 044054 (2021).
[17] D. Di Nuzzo, L. J. A. Koster, V. S. Gevaerts, S. C. Meskers, and R. A. Janssen, Adv. Energy Mater. **4**, 1400416 (2014).
[18] J. Kurpiers, T. Ferron, S. Roland, M. Jakoby, T. Thiede, F. Jaiser, S. Albrecht, S. Janietz, B. A. Collins, I. A. Howard, and D. Neher, Nat. Commun. **9**, 2038 (2025).
[19] S. Athanasopoulos, F. Schauer, V. Nádaždy, M. Weiß, F. J. Kahle, U. Scherf, H. Bässler, and A. Köhler, Adv. Energy Mater. **9**, 1900814 (2019).
[20] Y. Tamai, Polym. J. **52**, 691 (2020).
[21] D. Balzer and I. Kassal, Sci. Adv. **8**, eabl9692 (2022).
[22] X. K. Chen, D. Qian, Y. Wang, T. Kirchartz, W. Tress, H. Yao, J. Yuan, M. Hülsbeck, M. Zhang, Y. Zou, Y. Sun, Y. Li, J. Hou, O. Inganäs, V. Coropceanu, J. L. Bredas, and F. Gao, Nat. Energy **6**, 799 (2021).
[23] P. Bi, S. Zhang, Z. Chen, Y. Xu, Y. Cui, T. Zhang, J. Ren, J. Qin, L. Hong, X. Hao, and J. Hou, Joule **5**, 2408 (2021).
[24] L. Benatto, C. A. M. Moraes, G. Candiotto, K. R. A. Sousa, J. P. A. Souza, L. S. Roman, and M. Koehler,

J. Mater. Chem. A **9**, 27568 (2021).
[25] S. M. Falke, C. A. Rozzi, D. Brida, M. Maiuri, M. Amato, E. Sommer, A. D. Sio, A. Rubio, G. Cerullo, E. Molinari, and C. Lienau, Science **344**, 1001 (2014).
[26] W. Chi, J. Wu, Y. Dong, J. Wu, and Y. Zhu, Angew. Chem., Int. Ed. (2025). DOI: 10.1002/anie.202508690
[27] H. G. Duan, A. Jha, V. Tiwari, R. D. Miller, and M. Thorwart, Chem. Phys. **528**, 110525 (2020).
[28] S. Gélinas, A. Rao, A. Kumar, S. L. Smith, A. W. Chin, J. Clark, T. S. Van Der Poll, G. C. Bazan, and R. H. Friend, Science **343**, 512 (2014).
[29] A. C. Jakowetz, M. L. Böhm, J. Zhang, A. Sadhanala, S. Huettner, A. A. Bakulin, A. Rao, and R. H. Friend, J. Am. Chem. Soc. **138**, 11672 (2016).
[30] M. Brendel, S. Krause, A. Steindamm, A. K. Topczak, S. Sundarraj, P. Erk, S. Höhla, N. Fruehauf, N. Koch, and J. Pflaum, Adv. Funct. Mater. **25**, 1565 (2015).
[31] J. Sun, D. Li, J. Zou, S. Zhu, C. Xu, Y. Zou, Z. Zhang, and H. Lu, npj Comput. Mater. **10**, 181 (2024).
[32] B. Liu, H. Sun, J. W. Lee, Z. Jiang, J. Qiao, J. Wang, J. Yang, K. Feng, Q. Liao, M. An, B. Li, D. Han, B. Xu, H. Lian, L. Niu, B. J. Kim, and X. Guo, Nat. Commun. **14**, 967 (2023).
[33] S. Feng, Q. Ge, R. Zhou, Z. Zheng, W. Liang, and Y. Zhao, J. Chem. Phys. **163**, 024113 (2025).
[34] S. Zhang, J. Wang, S. Wen, M. Jiang, H. Xiao, X. Ding, N. Wang, M. Li, X. Zu, S. Li, C. Yam, B. Huang, and L. Qiao, Phys. Rev. Lett. **126**, 176401 (2021).
[35] J. Xiao, L. Peng, L. Gao, J. Zhong, Z. Huang, E. Yuan, V. Srinivasapriyan, S. F. Zhou, and G. Zhan, RSC Adv. **11**, 16600 (2021).
[36] N. Yang, S. Zhang, Y. Cui, J. Wang, S. Cheng, and J. Hou, Nat. Rev. Mater. **10**, 404 (2025).
[37] S. Feng, Y. C. Wang, W. Liang, and Y. Zhao, J. Phys. Chem. A **125**, 2932 (2021).
[38] S. Feng, Y. C. Wang, Y. Ke, W. Liang, and Y. Zhao, J. Chem. Phys. **153**, 034116 (2020).
[39] S. Feng, Y. C. Wang, W. Liang, and Y. Zhao, Phys. Chem. Chem. Phys. **24**, 2974 (2022).
[40] Y. Xu, Y. Zhao, and W. Liang, J. Phys. Chem. C **128**, 20253 (2024).
[41] Y. Xu, X. Huang, Y. C. Wang, Y. Zhao, and W. Liang, Phys. Chem. Chem. Phys. **26**, 6155 (2024).
[42] Y. C. Wang and Y. Zhao, Chin. J. Chem. Phys. **33**, 653 (2020).
[43] N. F. Ness and L. F. Burlaga, J. Geophys. Res.: Space Phys. **106**, 15803 (2001).
[44] F. Giustino, M. L. Cohen, and S. G. Louie, Phys. Rev. B **76**, 165108 (2007).
[45] F. Giustino, Rev. Mod. Phys. **89**, 015003 (2017).
[46] M. K. Nuraliev, O. D. Parashchuk, N. V. Tukachev, Y. A. Repeev, D. R. Maslennikov, O. V. Borshchev, Y. G. Vainer, D. Y. Paraschuk, and A. Y. Sosorev, J. Chem. Phys. **153**, 174303 (2020).
[47] Y. C. Wang, S. Feng, W. Liang, and Y. Zhao, J. Phys. Chem. Lett. **12**, 1032 (2021).
[48] Y. Ke and Y. Zhao, J. Chem. Phys. **146**, 174105 (2017).
[49] A. Hoshino, Y. Takenaka, and H. Miyaji, Acta Crystallogr. B Struct. Sci. Cryst. Eng. Mater. **59**, 393 (2003).
[50] P. E. Blöchl, O. Jepsen, and O. K. Andersen, Phys. Rev. B **49**, 16223 (1994).
[51] G. Kresse and J. Furthmüller, Comput. Mater. Sci. **6**, 15 (1996).
[52] T. Yanai, D. P. Tew, and N. C. Handy, Chem. Phys. Lett. **393**, 51 (2004).
[53] F. Weigend and R. Ahlrichs, Phys. Chem. Chem. Phys. **7**, 3297 (2005).
[54] P. J. Stephens, F. J. Devlin, C. F. Chabalowski, and M. J. Frisch, J. Phys. Chem. **98**, 11623 (1994).
[55] M. J. Frisch, G. W. Trucks, H. B. Schlegel, G. E. Scuseria, M. A. Robb, J. R. Cheeseman, G. Scalmani, V. Barone, G. A. Petersson, H. Nakatsuji, X. Li, M. Caricato, A. V. Marenich, J. Bloino, B. G. Janesko, R. Gomperts, B. Mennucci, H. P. Hratchian, J. V. Ortiz, A. F. Izmaylov, J. L. Sonnenberg, D. WilliamsYoung, F. Ding, F. Lipparini, F. Egidi, J. Goings, B. Peng, A. Petrone, T. Henderson, D. Ranasinghe, V. G. Zakrzewski, J. Gao, N. Rega, G. Zheng, W. Liang, M. Hada, M. Ehara, K. Toyota, R. Fukuda, J. Hasegawa, M. Ishida, T. Nakajima, Y. Honda, O. Kitao, H. Nakai, T. Vreven, K. Throssell, J. A. Montgomery, Jr., J. E. Peralta, F. Ogliaro, M. J. Bearpark, J. J. Heyd, E. N. Brothers, K. N. Kudin, V. N. Staroverov, T. A. Keith, R. Kobayashi, J. Normand, K. Raghavachari, A. P. Rendell, J. C. Burant, S. S. Iyengar, J. Tomasi, M. Cossi, J. M. Millam, M. Klene, C. Adamo, R. Cammi, J. W. Ochterski, R. L. Martin, K. Morokuma, O. Farkas, J. B. Foresman, and D. J. Fox, *Gaussian 16 Revision A.03*, Wallingford CT: Gaussian Inc., (2016).
[56] T. Lu, J. Chem. Phys. **161**, 082503 (2024).
[57] W. Humphrey, A. Dalke, and K. Schulten, J. Mol. Graph. **14**, 33 (1996).
[58] T. Meier, Y. Zhao, V. Chernyak, and S. Mukamel, J. Chem. Phys. **107**, 3876 (1997).
[59] J. C. Kirkwood, C. Scheurer, V. Chernyak, and S. Mukamel, J. Chem. Phys. **114**, 2419 (2001).
[60] R. F. Kelley, R. H. Goldsmith, and M. R. Wasielewski, J. Am. Chem. Soc. **129**, 6384 (2007).

DOI: 10.1063/1674-0068/cjcp2506086